

Journal of Materials Chemistry A

Materials for energy and sustainability

Accepted Manuscript

This article can be cited before page numbers have been issued, to do this please use: R. Shankar, M. Sachs, L. Francás, D. Lubert-Perquel, G. Kerherve, A. Regoutz and C. Petit, *J. Mater. Chem. A*, 2019, DOI: 10.1039/C9TA02793A.



This is an Accepted Manuscript, which has been through the Royal Society of Chemistry peer review process and has been accepted for publication.

Accepted Manuscripts are published online shortly after acceptance, before technical editing, formatting and proof reading. Using this free service, authors can make their results available to the community, in citable form, before we publish the edited article. We will replace this Accepted Manuscript with the edited and formatted Advance Article as soon as it is available.

You can find more information about Accepted Manuscripts in the [Information for Authors](#).

Please note that technical editing may introduce minor changes to the text and/or graphics, which may alter content. The journal's standard [Terms & Conditions](#) and the [Ethical guidelines](#) still apply. In no event shall the Royal Society of Chemistry be held responsible for any errors or omissions in this Accepted Manuscript or any consequences arising from the use of any information it contains.

Porous boron nitride for combined CO₂ capture and photoreduction

View Article Online

DOI: 10.1039/C9TA02793A

Ravi Shankar^a, Michael Sachs^b, Laia Francàs^b, Daphné Lubert-Perquel^c, Gwilherm Kerherve^d, Anna Regoutz^d, and Camille Petit^{a*}

^aBarrer Centre, Department of Chemical Engineering, Imperial College London, South Kensington Campus, Exhibition Road, London SW7 2AZ, United Kingdom

^bDepartment of Chemistry, Imperial College London, South Kensington Campus, Exhibition Road, London SW7 2AZ, United Kingdom

^cLondon Centre for Nanotechnology and Department of Materials, Imperial College London, South Kensington Campus, Prince's Consort Road, London SW7 2BP, United Kingdom

^dDepartment of Materials, Imperial College London, South Kensington Campus, Prince's Consort Road, London SW7 2BP, United Kingdom

*Corresponding author:

E-mail: camille.petit@imperial.ac.uk; Phone: +44 (0)20 7594 3182 (C. Petit)

AbstractView Article Online
DOI: 10.1039/C9TA02793A

Porous and amorphous materials are typically not employed for photocatalytic purposes, like CO₂ photoreduction as their high number of defects can lead to low charge mobility and favour bulk electron-hole recombination. Yet, with a disordered nature can come porosity, which in turns promotes catalyst/reactant interactions and fast charge transfer to reactants. Here, we demonstrate that moving from *h*-BN, a well-known crystalline insulator, to amorphous BN, we create a semiconductor, which is able to photoreduce CO₂ in a gas/solid phase, under both UV-vis and pure visible light, ambient conditions, without the need for cocatalysts. The material selectively produces CO and maintains its photocatalytic stability over several catalytic cycles. The performance of this un-optimized material is on par with that of TiO₂, the benchmark in the field. For the first time, we map out experimentally the band edges of porous BN on the absolute energy scale vs. vacuum to provide fundamental insight into the reaction mechanism. Owing to the chemical and structural tunability of porous BN, these findings highlight the potential of porous BN-based structures for photocatalysis and particularly solar fuels production.

Keywords: boron nitride, photocatalysis, CO₂ photoreduction, solar fuel, porous materials.

Introduction

View Article Online
DOI: 10.1039/C9TA02793A

With a push towards sustainable energy technologies, the share of renewables is projected to significantly increase in the years and decades to come.¹ Solar fuel production *via* photocatalysis represents one such energy generation route, allowing to directly take advantage of sunlight. Solar fuels include H₂ derived from water splitting and carbon-based molecules (*e.g.* CH₄, CO, CH₃OH, etc...) derived from CO₂ reduction. Literature on CO₂ photoreduction catalysts is comparatively less extensive than on H₂ and O₂ generation, owing to the significant thermodynamic and kinetic limitations of CO₂ reduction. In fact, about 40 years after the work of Inoue *et al.* (1979), TiO₂ remains the reference material in the field.² Researchers have looked at expanding the range of viable photocatalysts with works reported on derivatives of TiO₂, metal oxides, oxynitrides, carbon nitride, metal-organic frameworks and composites thereof.³⁻¹⁶ Overall, these studies concentrate on optimizing light absorption, preventing charge recombination, enhancing material robustness and controlling surface-catalysed reaction mechanisms and selectivity. For the most part, they focus on metal-based crystalline materials with low porosity. The latter feature prevents the development of gas phase CO₂ photoreduction, which would allow integrated CO₂ capture and conversion set-ups. In addition, the usage of rare metals either as part of the photocatalyst or as co-catalysts limits large-scale deployment.

Here, taking into account the advent of graphitic carbon nitride and other carbonaceous materials, we turn our attention to porous boron nitride (BN).¹⁷⁻²⁶ Porous BN exhibits key features of an ideal photocatalyst, yet it has never been studied for CO₂ photoreduction. The compelling features of BN include its metal-free nature as well as its tuneable chemistry and structure that *a priori* allow for a tailored band structure.²⁷⁻²⁹ Porous BN is the amorphous analogue of hexagonal boron nitride (*h*-BN), a wide band gap insulator (~5.5 eV).³⁰ Doping of this robust material and its utilisation in composites have been employed to reduce the band gap and allow the formation of heterojunctions, respectively.³¹⁻³⁴ Today, the only reports of BN-based materials for CO₂ photoreduction are on carbon-doped BN³⁵⁻³⁸, which

have since been shown to be unstable in the presence of moisture owing to the breaking of the B-C bond.^{39, 40}

Herein, we report a porous BN material as both CO₂ adsorbent and CO₂ photoreduction catalyst under both UV and visible light. We explain how the structure and chemistry of the materials control its adsorptive, optoelectronic, photophysical, paramagnetic and photocatalytic properties. Further, we delve deeper into the photochemistry of porous BN by determining, and aligning the position of the conduction (CB) and valence (VB) band edge as well as the Fermi level on the absolute energy scale vs. vacuum to elucidate the CO₂ photoreduction reaction mechanism. Prior to this study, the band edges of porous BN were yet to be obtained experimentally. This work paves the way for the creation of a new CO₂ photocatalyst platform.

Results and discussion

We synthesised porous BN based on the previous work of Marchesini *et al.* (2017), whose approach relies on a bottom-up pyrolytic synthesis at elevated temperatures using a mixture of boric acid, melamine and urea.⁴¹ To gain insight into the morphology and structure of the material, we collected high resolution transmission electron microscopy (HRTEM) and scanning electron microscopy (SEM) images, as well as X-ray diffraction (XRD) patterns (Figures 1a-c). Both techniques confirm the low degree of crystallinity of porous BN as opposed to *h*-BN. As seen on the HRTEM images, the range of stacked 2D layers is limited in porous BN (Figure 1b) and the SEM images depict a densely packed pore structure (Supplementary Figure 1). In fact, the XRD patterns confirm the turbostratic nature of the material with only broad peaks at 2θ values of 26° and 44°, corresponding to the (002) and (100) planes, respectively. This contrasts with the sharp peaks for *h*-BN that indicate long-range 3D/graphitic order. The d-spacing calculated from the TEM images and XRD peak (002) for *h*-BN and porous BN is 3.4 Å and 3.5 Å, respectively.^{42, 43 44} The d-spacing in porous BN is only relevant to the pseudo-crystalline regions of the material. To characterize the structural

features of the material at the micro/nano-scale, we analysed the specific surface area and porosity through nitrogen sorption at $-196\text{ }^{\circ}\text{C}$ (Figure 1d for isotherms, Supplementary Table 1 for textural parameters). The porous BN sample displays a BET equivalent specific surface area of $1585\text{ m}^2\text{ g}^{-1}$ and total pore volume of $1.10\text{ cm}^3\text{ g}^{-1}$, which is considerably larger than those for *h*-BN ($3\text{ m}^2\text{ g}^{-1}$ and $0.006\text{ cm}^3\text{ g}^{-1}$). The type I/IV isotherm with a type H3/H4 hysteresis loop observed for porous BN indicates the presence of slit-shaped micro- and mesopores. The high surface area of porous BN is key for interfacial phenomena, enhancing access to active CO_2 absorption and reduction sites. This is particularly important in gas phase schemes like the one proposed here, where CO_2 reduction is limited by the ability of the molecules to be adsorbed on the catalyst, close to the catalytic sites.

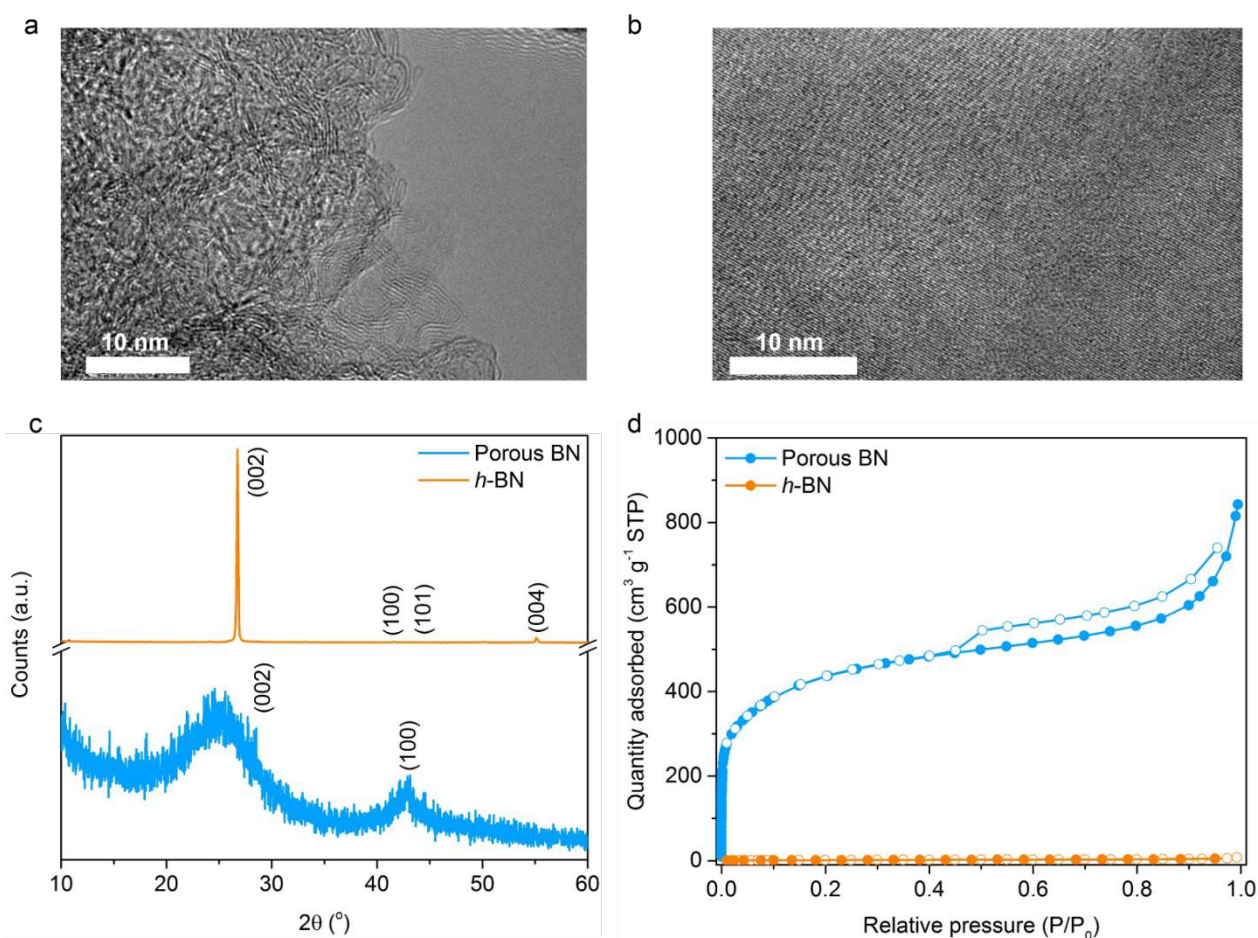


Figure 1 | Structure and morphology of porous BN sample compared to *h*-BN. (a) HRTEM image of the as-synthesized porous BN sample highlighting the porous morphology through the absence of stacked layers and the presence of wide crystalline domains, (b) HRTEM image of *h*-BN, taken for comparison, illustrating the high degree of crystallinity with a large number of stacked, well-ordered 2D layers, (c) Powder XRD patterns of porous BN and *h*-BN, (d) N₂ sorption isotherms for porous BN and *h*-BN measured at -196 °C.

View Article Online
DOI: 10.1039/C9TA02793A

We characterised the chemical structure and bonding types of the porous BN through Raman spectroscopy, Fourier transform infrared spectroscopy (FT-IR), EDX, and X-ray photoelectron spectroscopy (XPS) (Figure 2 and Supplementary Figures 2 and 3). Again, we used *h*-BN here as a reference material. Both porous BN and *h*-BN exhibit a strong Raman peak at $\sim 1370\text{ cm}^{-1}$, corresponding to the counter-phase B-N E_{2g} vibration mode within the BN structure (Supplementary Figure 2).^{45, 46} We observed the two characteristic IR bands of BN at $\sim 1380\text{ cm}^{-1}$ (in-plane B-N transverse stretching) and $\sim 800\text{ cm}^{-1}$ (out-of-plane B-N-B bending) in both samples,⁴⁷ while no B-O bands, typically observed at $\sim 1000\text{ cm}^{-1}$, are noted (Figure 2a).^{28, 48} Yet, elemental mapping conducted using SEM EDX points to the presence of oxygen homogeneously distributed through the structure (Figure 2b). To gain further insight into the relative atomic surface composition and chemical states of the elements, we collected high resolution core level spectra through XPS. The analysis indicates a significant proportion (10 at. % \pm 1 at. %) of oxygen in porous BN (Figure 2c) with a peak at 533.1 eV (Supplementary Figure 3). We attribute this peak to boron oxynitride (B-O_x-N_y) species, which stems from the in-plane substitution of oxygen atoms into the BN lattice, as we have described in a prior study.^{29, 49} Oxygen atoms were observed on *h*-BN and are most likely related to edge hydroxyl groups (Figure 2c). The formation of BN is confirmed through the fitted core level spectra of the B 1s and N 1s and show the presence of B-N bonds (191.0 eV for B 1s and 398.5 eV for N 1s, Supplementary Figure 3).^{50, 51} We also observe shake-up satellite peaks the B 1s and N 1s core level spectra for porous BN (Supplementary Figure 3), which provides evidence for the formation of a sp²-hybridised hexagonal BN phase.⁵²⁻⁵⁴ The

carbon content in the sample was comparatively much lower ($\sim 3 \text{ at. } \% \pm 1 \text{ at. } \%$) and is linked to the presence of adventitious carbon impurities, *i.e.* not part of the material. Oxygen atoms can enhance CO_2 adsorption^{55, 56} and can also lead to reduced band gap, as indicated by both computational and experimental work.^{28, 57, 58} Both aspects are important in the context of CO_2 capture and photoconversion.

Next, we probed the optoelectronic properties of porous BN through UV-vis diffuse reflectance spectroscopy. The absorption spectrum (Figure 2d) of the material clearly indicates a red-shift when moving from *h*-BN to porous BN, with the absorption edge moving from 215 nm to 290 nm. From the Tauc plot of the transformed Kubelka-Munk function against photon energy (Supplementary Figure 5a), the sample exhibits a UV-range band gap of $4.21 \text{ eV} \pm 0.05 \text{ eV}$, significantly lower than that of *h*-BN ($\sim 5.51 \text{ eV} \pm 0.02 \text{ eV}$) (Supplementary Figure 5b). These results point to the creation of a semiconducting porous BN material. At this stage, we cannot infer whether the semiconducting property is related to the presence of functional groups, their specific location on the BN nanosheets or the introduction of porosity.

We next collected time-resolved photoluminescence spectra to characterise the excited state properties of our porous BN. We compare the results to the behaviour of another metal-free photocatalyst, whose layered structure is similar to that of *h*-BN: graphitic carbon nitride (*g*- C_3N_4). For both materials, photoluminescence decay components are extracted by global analysis of the time-resolved spectra, where each component is characterised by a certain photoluminescence spectrum and decay (details described in Supplementary Figure 6). For *g*- C_3N_4 , a single component with a spectrum shown in Figure 2e is found, following power law decay kinetics $\propto t^{-1.6}$. This observation is in good agreement with a study by Godin *et al.* (2017) where power law decay kinetics $\propto t^{-1.5}$ were observed over a wide range of time scales in *g*- C_3N_4 .⁵⁹ Such power law kinetics are indicative of recombination *via* trapping-detrapping steps, and this component can thus be assigned to shallowly trapped charges (charges trapped at energies close to the band edge).^{59, 60} In contrast, two components are

found for porous BN (Figure 2f). An exponentially decaying component (time constant $\tau = 1.5$ ns) dominates at early times, which can be assigned to excitons (bound electron-hole pairs) based on the exponential decay and the relatively narrow photoluminescence spectrum close to the band gap transition. At later times, a second component following the same power law decay kinetics $\propto t^{-1.6}$ as in g-C₃N₄ dominates, analogously assigned to shallowly trapped charges. These results demonstrate that BN exhibits longer exciton lifetimes than g-C₃N₄ and that shallowly trapped charges follow the same decay kinetics in porous BN and g-C₃N₄. We note that charge yields, which could not be compared for the used samples, might provide further insights into photocatalytic activities.

The presence of oxygen atoms in the interior structure of porous BN, arising from the substitution of nitrogen atoms, results in unpaired electrons upon in-plane bonding with boron atoms. This in turn yields associated paramagnetic properties of the porous BN catalyst, which we probed through room temperature electron paramagnetic resonance (EPR) measurements and compared to *h*-BN as a reference. We detected a strong EPR signal at a magnetic field of approximately 342 mT with a calculated *g*-value of 2.0032 (Figure 2g). This value is in good agreement with literature values.^{28, 35} In comparison, no resonance peak was observed for *h*-BN. This paramagnetic signature of the material indicates the presence of unpaired free electrons in porous BN, which stems from the isolated, conjugated –OB₃ bonding pattern.²⁸ Functional groups, such as edge hydroxyl groups, or other bonding patterns such as –O₂B are not capable of generating unpaired electrons, and therefore would not contribute towards paramagnetism. Hence, this confirms the presence of interior-substituted oxygen atoms in porous BN. The resonance signal at a *g*-value of 2.0032 for porous BN in Figure 2g exhibits a symmetric signal, which demonstrates an isotropic *g* of a uniform electron species. An approximate 30% increase in the EPR peak intensity for porous BN was observed when the sample was irradiated using UV-vis light, as shown in Figure 2h. Previous work has attributed the contribution to the generation of electron-hole pairs.³⁵ This would correspond to the short-lived photoinduced

excitons, which were previously assigned to the exponential decay component of the photoluminescence spectra in Figure 2f. However, the signal enhancement could also be due to the release of the trapped charges under illumination, therefore time-resolved measurements would be required to discriminate between these two interpretations. These findings nonetheless indicate porous BN is able to function as a semiconductor upon excitation.

[View Article Online](#)
DOI: 10.1039/C9TA02793A

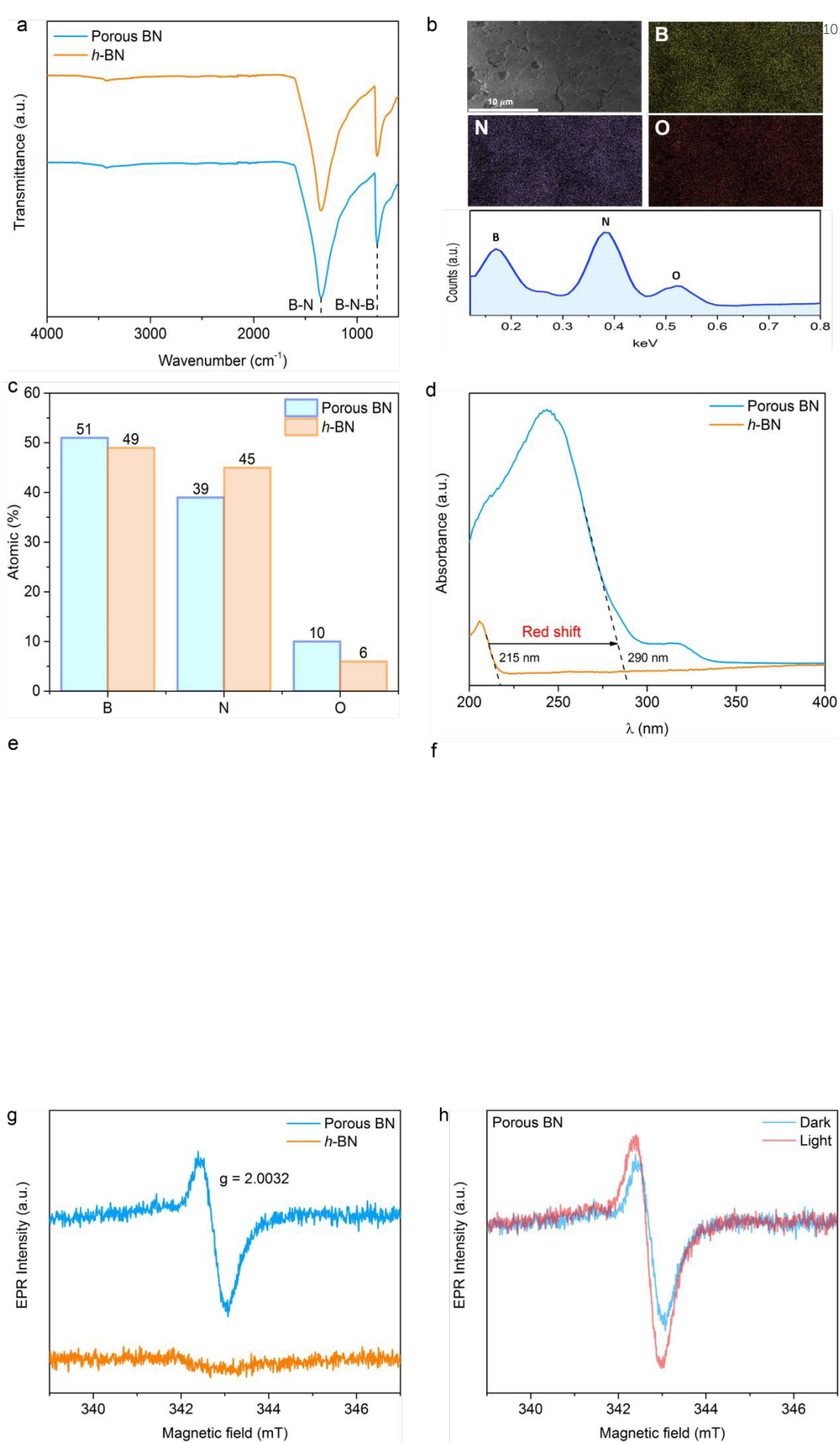
View Article Online
DOI: 10.1039/C9TA02793A

Figure 2 | Chemical, electronic, photophysical and paramagnetic characterisation of porous BN as compared to *h*-BN and *g*-C₃N₄. (a) FT-IR spectra of as-synthesized porous BN, with key characteristic bands highlighted, and *h*-BN as a reference, (b) SEM image, EDX spectrum and elemental mapping for porous BN showing the homogeneous distribution of the elements throughout the structure, (c) Relative atomic composition of porous BN obtained through XPS analysis, (d) Absorption spectrum of the porous BN sample compared to that of *h*-BN, (e, f) Component spectra extracted by global fitting of time-resolved photoluminescence spectra for graphitic carbon nitride (*g*-C₃N₄) and porous BN, obtained upon excitation at 282 nm. Models used for the global fits are described in the Supporting Information, (g) Room temperature EPR spectra for porous BN compared to that of *h*-BN with the *g*-value indicated, (h) Comparison of the EPR spectra for porous BN under dark and UV-vis light irradiation conditions (300 W Xe arc lamp, 25 °C).

Prior to photocatalytic testing, we measured the CO₂ adsorption capacity of the material at the reaction conditions (25 °C, 0-1 bara) and compared to 'reference' materials, *i.e.* TiO₂ P25, *h*-BN and carbon nitride. We have selected these reference materials for the following reasons. TiO₂ P25 is a benchmark commercial material in the field, which enables comparison with other groups' work, despite differences in experimental set-ups. Being a commercial material, P25 acts as an internal reference and its use for comparison is in part of the guidance in the field.⁶¹ Graphitic carbon nitride is the closest material in terms of chemistry and structure to porous BN and a well-known visible light photocatalyst. Some of the photophysics properties and behaviour of porous BN are likely to bear resemblances with those observed in carbon nitride. *h*-BN is the most well-known BN form due to its long standing use in industry as a lubricant. It's the crystalline and insulating nature may have acted as barriers for researchers to explore the semiconducting behaviour of other forms of BN. We have also included results from a metal organic framework (MOF, see Supplementary Figure 8 as a representative of a porous polymeric material. The chemistry and photophysics are very however very different between BN and MOF.

Unsurprisingly, porous BN adsorbs significantly more CO₂ than the reference materials (Figure 3a), most likely due to its higher porosity (Supplementary Tables 1 and 2). Other groups have already reported the use of porous BN as an adsorbent for CO₂, with similar capacities reported.^{41, 55, 62, 63} Next, we tested porous BN and the reference materials for the gas phase photoreduction of CO₂ under UV-vis and pure visible irradiation, without doping or the presence of a co-catalyst. For all materials, after an irradiation time of 5 hours, the only product observed is CO. The CO₂ adsorption capacities at 25 °C and specific CO evolution rates of all of the materials investigated in this study are tabulated in Table 1. Under these conditions, porous BN drove the photoreduction of CO₂ with an average specific CO production rate of 1.16 μmol g⁻¹ h⁻¹ (Figure 3b). Under UV-vis irradiation, porous BN exhibits a higher specific CO production rate than those for the reference materials. We attribute the significant increase in CO production going from *h*-BN to porous BN to the increase in surface area and porosity as well as the greater light harvesting efficiency. We note that the surface area of g-C₃N₄ is much lower than that of porous BN. Should its surface area be increased, a higher performance might be observed. Porous BN is surpassed by g-C₃N₄ and P25 using visible irradiation, which is to be expected given the lower band gaps of these material (2.72 eV and 3.20 eV, respectively). Such low band gap may be attainable in BN after significant O doping as suggested in the literature^{28, 57, 58}. Interestingly both TiO₂ and porous BN exhibit visible light activity despite their relatively band gaps. The visible light activity of P25 has been observed by other research groups worldwide and is attributed to the presence of shallow trap states and mixed-phase (rutile-anatase) nanoclusters that extends the photoactivity of P25 TiO₂ to the visible region.⁶⁴⁻⁶⁶ For porous BN, the origin of this visible light activity is still unclear. At present, we speculate that the presence of trap states, namely the shallow trapped state shown in Figure 2f, is responsible for the visible light activity. To investigate this further, we tested porous BN for CO₂ photoreduction under the same setup using a 550 nm long pass visible filter. No CO or other gaseous products were detected for $\lambda > 550$ nm (Figure 3b and Supplementary Table 2). As porous BN evolves CO in the visible region for $400 < \lambda < 550$ nm, over which the shallow trapped

charge is present, we postulate that this contributes to the visible light activity of the material. Further experimental studies are planned in a follow up to this study to identify the nature of these trap states. These trap states could originate from N vacancies or O substituting N atoms in porous BN. We note that porous BN can also photoreduce CO₂ to CO with a 100% selectivity using H₂O rather than H₂ as the sacrificial agent (Figure 3b).

We confirmed the origin of CO through a number of control tests: absence of catalyst, dark mode, N₂/H₂ atmosphere (Supplementary Table 2). All supported the fact that the source of the CO evolved stems from the photocatalytic reduction of CO₂. To further substantiate this claim, we carried out isotopic experiments using ¹³CO₂. Aside from ¹³CO₂ being used as the feed gas in tandem with H₂ as the sacrificial agent, we maintained the same catalyst preparation method and reaction conditions from the original system. The gas chromatogram corresponding to the ¹³CO peak and the mass spectra for the photocatalytic ¹³CO₂ reduction system are presented in Supplementary Figure 8. The results point to the formation of ¹³CO and provides direct evidence that the origin of the evolved CO is indeed from the reduction of CO₂ itself.

The kinetic study (Figure 3c) points to a constant CO evolution rate over a 6 hour testing period, which shows that the catalyst was able to maintain its photoactivity throughout the course of the reaction. We tested further the recyclability of the catalyst over 3 cycles under UV-vis irradiation (Figure 3d). We observed a 14% decrease in CO production after the third cycle (Figure 3d).

Further, we checked the stability of the material through XRD pattern of the used catalyst and observed a slight increase in crystallinity after CO₂ photoreduction (Supplementary Figure 9). This finding suggests that amorphous domains of the material degraded upon reaction. This is supported by N₂ sorption tests, which showed a 25% decrease in porosity after reaction using H₂ or H₂O. Notably though, the porous BN sample still maintained a high surface area and porosity of 1196 m² g⁻¹ (1190 m² g⁻¹ for H₂O) and 1.01 cm³ g⁻¹ (0.94 cm³ g⁻¹ for H₂O, Supplementary Table 1). We did not observe any distinct changes in the FT-IR

spectrum of the sample after undergoing a CO₂ photoreduction cycle (Supplementary Figure 9). Similarly, we did not observe any changes in the sample morphology (Supplementary Figure 1) or the relative atomic composition of the sample after undergoing a CO₂ photoreduction cycle (Supplementary Figure 4).

To further demonstrate that porous BN can facilitate the gas phase photoreduction of CO₂ as a photocatalyst, we resolved the band structure of the material, specifically the positions of the valence band (VB) and conduction band (CB) on the absolute energy scale. Importantly, despite numerous reports of the band gap, which only gives the relative positions of the CB and VB, the band positions for either porous BN or *h*-BN on the absolute scale are yet to be reported in the literature. We first conducted valence band XPS measurements on porous BN to determine the relative distance between the Fermi level (E_F) and the onset of the valence band, also known as the valence band offset. The average valence band offset was determined to be $3.05 \text{ eV} \pm 0.02 \text{ eV}$ (Figure 3e). High resolution core level spectra (B 1s, N 1s, C 1s, and O 1s) were simultaneously measured along with the valence band spectrum for porous BN and no effects of charging were observed. Aligning the complete band structure of porous BN on the absolute energy scale requires knowledge of the absolute position of the Fermi level (E_F). This can be obtained by conducting work function measurements to measure the secondary electron cut-off through photoelectron spectroscopy. The work function of the material (Φ) gives the distance between Fermi level of the material (E_F) and the absolute vacuum level (0 eV). We note that work function measurements conducted through photoelectron spectroscopy are extremely sensitive to subtle changes in experimental conditions and necessitate the preparation of a well-controlled, homogeneous surface. To negate the effects of surface roughness, a known mass of porous BN was pelletized to form a thin homogeneous surface. Further, to account for potential variations across the surface of the material, the work function was measured at four different locations and an average was taken (Supplementary Figure 10). The average work function (Φ) for porous BN was determined to be $2.90 \text{ eV} \pm 0.30 \text{ eV}$. Therefore, as the

absolute vacuum level is at 0 eV (the datum for the absolute energy scale), it follows that the Fermi level of the sample lies at $2.90 \text{ eV} \pm 0.30 \text{ eV}$. Using the valence band offset of $3.05 \pm 0.02 \text{ eV}$ in Figure 3e), the valence band must lie at $5.95 \text{ eV} \pm 0.32 \text{ eV}$ on the absolute energy scale. Hence, if the band gap of the material (E_G) is $4.21 \text{ eV} \pm 0.05 \text{ eV}$ (Supplementary Figure 5), the conduction band is positioned at $1.74 \text{ eV} \pm 0.37 \text{ eV}$ on the absolute energy scale. To align the absolute energy scale vs. vacuum with the redox potential scale vs. the standard hydrogen electrode (SHE), we used the fact that 4.44 eV on the former corresponds to 0.00 V on the latter at 298 K.^{67, 68} In doing so, we can align the known redox potentials for CO_2/CO (-0.53 V) and H^+/H_2 (0.00 V) reported in the literature on the absolute energy scale.⁶⁹ Combining this data with the values calculated from the valence band and work function measurements yields the full band structure for porous BN shown in Figure 3f. A detailed derivation and error propagation analysis is presented in the supplementary information. The key conclusions from this are two-fold. Firstly, the CB and VB of porous BN do indeed straddle the redox potentials for CO_2/CO and H^+/H_2 , respectively, in the photoredox system with a reduction overpotential ($\eta_{\text{CO}_2/\text{CO}}$) of $2.16 \pm 0.37 \text{ eV}$. This confirms that the band structure of porous BN are aligned to provide a sufficient thermodynamic driving force to facilitate the reduction of CO_2 to CO .

In addition, the separation of the Fermi level (E_F) to the CB is $1.16 \text{ eV} \pm 0.34 \text{ eV}$, whilst the distance from the former to the VB is $3.05 \text{ eV} \pm 0.02 \text{ eV}$ (Figures 3e and 3f). As the Fermi level lies closer to the CB than the VB, porous BN behaves as an n-type semiconductor. Therefore, electrons are the major charge carriers in the photocatalyst, which is ideally suited to fulfilling the aim of CO_2 conversion through gas phase photoreduction. To conclude, the analysis conducted herein shows that the band structure of porous BN enables it to be an ideal catalyst to facilitate gas phase CO_2 photoreduction and further substantiates the claim that the CO evolved is indeed due to the action of the porous BN catalyst itself.

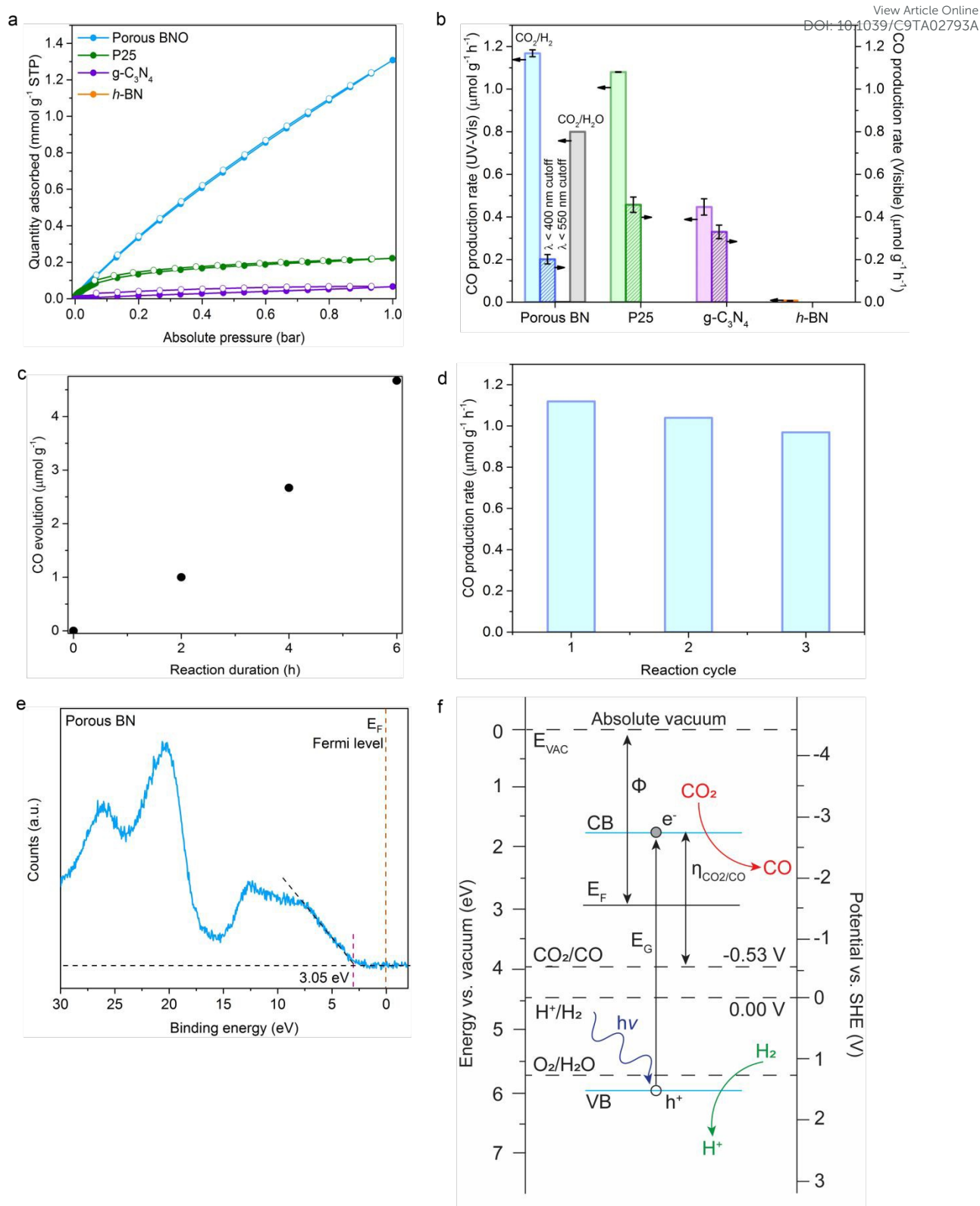


Figure 3 | Photocatalytic testing of the porous BN sample. (a) CO₂ adsorption isotherms collected at 25 °C for the materials investigated in this study (note the isotherm for *h*-BN is directly overlapped by that of *g*-C₃N₄), **(b)** Specific production rate of CO for porous BN, compared to TiO₂ P25, *h*-BN and carbon nitride (*g*-C₃N₄) as reference materials, under UV-

vis and pure visible light irradiation and H₂ or H₂O as sacrificial agents (300 W Xe arc lamp 9.5 cm distance from catalyst to lamp source, 5 hours, 25 °C). Intensity at the catalyst surface was 53800 W m⁻² without the UV-filter and 53100 W m⁻² with the UV filter ($\lambda < 400$ nm), (c) Photocatalytic CO evolution from porous BN as a function of time, (d) CO evolution from porous BN repeated over three 5 hour photocatalytic cycles, (e) Valence band XPS spectrum for porous BN to ascertain the distance between the Fermi level and valence band maximum, (f) Band structure for porous BN on the absolute energy scale vs. vacuum with the conduction and valence bands, Fermi level, and redox potentials for CO₂/CO, H⁺/H₂ and O₂/H₂O illustrated.

Table 1. CO₂ adsorption capacities (25 °C) and specific CO evolution rates of the materials investigated in this study.

Sample	CO ₂ adsorption capacity (mmol g ⁻¹ STP)	CO evolution rate (UV-Vis) ($\mu\text{mol g}^{-1} \text{h}^{-1}$)	CO evolution rate (Visible) ($\lambda > 400$ nm) ($\mu\text{mol g}^{-1} \text{h}^{-1}$)
Porous BN	1.22	1.17 \pm 0.02	0.20 \pm 0.02
P25	0.21	1.08 \pm 0.01	0.46 \pm 0.04
g-C ₃ N ₄	0.07	0.45 \pm 0.04	0.33 \pm 0.03
h-BN	0.03	0.01 \pm 0.01	n.d

n.d – none detected

In summary, we investigate a new material platform based on porous BN material that is able to facilitate combined CO₂ capture and photoreduction in a simple gas/solid phase set-up under ambient conditions, without the use of co-catalysts. Unlike its crystalline counterpart, porous BN exhibits semiconducting behaviour and can photoreduce CO₂ to CO under both UV-vis and visible irradiations, with evolution rates higher than the benchmark in the field, *i.e.* P25 TiO₂. Porous BN exhibits a steady CO evolution rate over a single cycle and maintained about 85% of its initial performance over multiple catalytic reactions. We present, for the first time, the complete band structure of porous BN to show that the material behaves as an n-type semiconductor, with the conduction and valence bands straddling the redox potentials for CO₂/CO and H⁺/H₂. Given the chemical and structural tunability of this material, there is considerable scope to expand the photocatalyst functionality to the visible-

light region, and increase its rate performance. This would constitute a major stride in the field of solar fuels synthesis.

View Article Online
DOI: 10.1039/C9TA02793A

Methods

Synthesis of porous BN. In a typical synthesis, boric acid (H_3BO_3 , ACS reagent, 99.0 %, Sigma-Aldrich), urea ($\text{CH}_4\text{N}_2\text{O}$, molecular biology grade, Sigma-Aldrich), and melamine ($\text{C}_3\text{H}_6\text{N}_6$, ACS reagent, 99.0 %, Sigma-Aldrich), with a 1:1 molar ratio of boric acid to melamine and 1:5 molar ratio of boric acid to urea were mechanically mixed together and finely ground for 5 minutes in an agate mortar to form a homogeneous powder. The finely ground powder was subsequently transferred to an alumina boat crucible, which was placed in a horizontal tubular furnace. The sample was initially degassed at ambient temperature for 3 hours under an inert nitrogen atmosphere (flow rate of $250 \text{ cm}^3 \text{ min}^{-1}$). Once the degas was complete, the nitrogen flow rate was decreased to $50 \text{ cm}^3 \text{ min}^{-1}$, and the sample was heated from ambient temperature to $1050 \text{ }^\circ\text{C}$ with a ramp rate of $10 \text{ }^\circ\text{C min}^{-1}$. This steady-state temperature was maintained for 3.5 hours, after which the samples were allowed to naturally cool to room temperature, whilst maintaining the same nitrogen flow rate. Upon completion of the synthesis, a porous white powder was obtained. The reference materials, *h*-BN and P25 TiO_2 were industrially synthesised and obtained as follows: *h*-BN (Tres BN, max. particle size 74 nm) and P25 TiO_2 (Sigma Aldrich, >99.5%, 21 nm primary particle size).

Synthesis of g- C_3N_4 . In a typical synthesis, 12 g of melamine ($\text{C}_3\text{H}_6\text{N}_6$, ACS reagent, 99.0 %, Sigma-Aldrich) were weighed and transferred to an alumina crucible, which was placed in a muffle furnace. The sample was heated from ambient temperature to $560 \text{ }^\circ\text{C}$ with a ramp rate of $5 \text{ }^\circ\text{C min}^{-1}$. This steady-state temperature was maintained for 4 hours, after which the samples were allowed to naturally cool to room temperature. Upon completion of the synthesis, a yellow solid product was obtained, which was subsequently ground in an agate mortar to form a fine, homogeneous powder.

Characterization. For FT-IR analysis, the samples were first ground to a powder using an agate mortar. Subsequently, the spectra were obtained in the range of 500 – 4000 cm^{-1} using a Perkin-Elmer Spectrum 100 FT-IR spectrometer equipped with an attenuated total reflectance (ATR) accessory. X-ray photoelectron spectroscopy (XPS) to determine the relative elemental composition of the samples, the chemical states of the elements, the valence band off-set and secondary electron cut-off was conducted using a Thermo Scientific K-Alpha⁺ X-ray Photoelectron Spectrometer equipped with a MXR3 Al $K\alpha$ monochromated X-ray source ($h\nu = 1486.6$ eV). The samples were initially ground and mounted onto an XPS sample holder using a small rectangular piece of conductive carbon tape. The X-ray gun power was set to 72 W (6 mA and 12 kV). Survey scans were acquired using 200 eV pass energy, 0.5 eV step size and 100 ms (50 ms x 2 scans) dwell times. All of the high resolution core level spectra (B 1s, N 1s, C 1s, and O 1s) were obtained using a 20 eV pass energy and 0.1 eV step size. The valence band spectra were obtained using a 15 eV pass energy and 0.05 eV step size. The results were analysed using the Thermo Avantage data analysis program. Powder X-ray diffraction (XRD) was performed using a PANalytical X'Pert Pro X-ray diffractometer in reflection-transmission mode with a spinning stage (2 revolutions/second). An anode voltage of 40 kV and emission current of 20 mA were chosen as the operating conditions using a monochromatic Cu- $K\alpha$ radiation source ($\lambda = 1.54178$ Å). The X'Celerator silicon strip detector was used in the diffractometer. Nitrogen and CO_2 sorption isotherms were measured using a porosity and surface area analyser (Micrometrics 3 Flex) at -196 °C and 25 °C, respectively. The samples were initially degassed overnight at 120 °C at approximately 0.2 mbar pressure. Subsequently, prior to the sorption isotherm measurement, the samples were degassed in-situ for 4 hours at 120 °C. The equivalent specific surface areas of the samples were determined using the Brunauer-Emmett-Teller (BET) method.⁷⁰ The total pore volume was ascertained from the volume of N_2 adsorbed at a relative pressure (P/P_0) of 0.97. The micropore volume was determined using the Dubnin-Radushkevich model. Transmission

Electron Microscopy (TEM) images were collected on a JEOL 2100Plus with 200 kV acceleration voltage. The samples were previously dispersed in ethanol and deposited on a carbon holey grid. SEM-EDX analysis was performed on an Auriga Zeiss microscope at 5 keV for both imaging and EDX analysis. The powder samples were compressed on a carbon tape and coated with 10 nm of gold.

Photocatalytic reduction of CO₂. A gas/solid photoreactor setup was assembled to conduct the photocatalytic reduction of CO₂. The as-synthesised, finely ground porous BN photocatalysts were deposited on a circular metal disc with a fixed area of 9.6 cm². To do so, 30 mg of porous BN powder was added to 1.5 mL of ethanol and stirred rapidly to form a homogeneous suspension, which was drop casted onto the sample holder. Research grade (99.999%) CO₂ and H₂ (99.9995%, Peak Scientific PH200 hydrogen generator) were flowed at controlled rates using mass flow controllers (Omega Engineering, 0–50 mL/min). Firstly, the photoreactor (35 cm³) was vacuumed and replenished with a gas mixture of CO₂ and H₂ (1.5 vol/vol ratio) ten times. The same gas mixture of CO₂ and H₂ was subsequently passed over the catalyst bed in the photoreactor for 15 residence times before it was sealed at 1.25 bara and irradiated for 5 hours. For experiments in which water vapour was used as the sacrificial reductant, this was generated from a saturator at room temperature (20 °C) providing a CO₂/H₂O ratio of around 40. Similarly, the photoreactor (35 cm³) was vacuumed and replenished with a gas mixture of CO₂ and H₂O ten times. A xenon arc lamp (300 W, $\lambda > 325$ nm, LOT Quantum Design), equipped with a water filter was used as the irradiation source with the distance from the lamp to the sample being 9.5 cm and the intensity at the catalyst surface measured to be 53800 W m⁻². A long pass UV filter ($\lambda < 400$ nm) (LOT Quantum Design) and a long pass visible filter ($\lambda < 550$ nm) (Thor Labs) were used to conduct the tests under visible light irradiation and the lamp emission spectra, both with and without the UV filters, are provided in Supplementary Figure 7. The evolved gases were detected by a gas chromatograph (GC, Agilent Technologies) with HayeSep and molecular sieve columns in series, and thermal conductivity (TCD) and flame ionisation (FID)

detectors. During the recyclability tests to assess the photostability of the materials, the aforementioned process was repeated after each 5-hour irradiation cycle without opening the photoreactor. In addition, isotopic tracing experiments were performed with $^{13}\text{CO}_2$ (BOC, >98% atom $^{13}\text{CO}_2$ compared to $^{12}\text{CO}_2$, >99%).

Time-resolved photoluminescence. Time-resolved emission experiments were conducted using a DeltaFlex time-resolved single photon counting system (Horiba) equipped with a PPD-650 detection module (Horiba) and a 282 nm JI-IBH NanoLED (1 ns pulse width, Horiba) excitation source. The acquired time-resolved emission spectra were analysed using a custom-built global analysis routine by fitting each dataset to a model (described in further detail in the Supporting Information), including convolution with the measured instrument response function.

Electron paramagnetic resonance (EPR) spectroscopy. EPR experiments were acquired using a Bruker Elexsys E580 CW EPR spectrometer operating at X-band frequencies (9–10 GHz/0.3 T), equipped with a Bruker ER4118-X MD5 resonator. The microwave frequencies used were 9.61 GHz with microwave power 2mW and in the detection sequence a 100kHz modulation with 2G amplitude was used. Light measurements of the BN sample was carried out under direct illumination of a 300W Xe arc lamp. All spectra were recorded at room temperature in air atmosphere in 4mm EPR suprasil tubes.

Work function measurements. The work function of porous BN was determined by measuring the secondary electron cut-off in the low kinetic energy region using a Thermo Scientific K-Alpha⁺ X-ray Photoelectron Spectrometer equipped with a MXR3 Al K α monochromated X-ray source ($h\nu = 1486.6$ eV). A known mass (100 mg) of sample was pelletized to form a thin, homogeneous pellet, which was clipped to the sample holder. The sample holder contained a clean gold standard sample, which was used as a reference material to ensure correct calibration. A sample bias of -30 V was applied to the samples using the ion gun and the cut-off spectra were obtained using a pass energy of 10 eV. To

account for potential variations across the surface of the material, the work function was measured at four different locations and an average was taken.

[View Article Online](#)

DOI: 10.1039/C9TA02793A

Acknowledgements

The authors would like to thank S. Marchesini for her help in producing the TEM images, to A. Crake for his technical input in the photocatalytic testing and isotopic testing, to A. Hankin for her help in measuring the lamp emission spectra, to L. Malms and F. Xie for their help in obtaining the UV-Vis diffuse-reflectance measurements. The authors would also like to acknowledge the funding from EPSRC through the Doctoral Partnership fund (1855454), which made this research possible, as well as the EPSRC equipment funding for SPIN-Lab (EP/P030548/1). AR acknowledges support from Imperial College for her Imperial College Research Fellowship. We also acknowledge support from the Department of Chemical Engineering at Imperial College London.

Declaration

The authors declare that there are no competing financial interests.

References

1. G. Centi; E. A. Quadrelli; S. Perathoner. *Energy & Environmental Science*, 2013, **6**, 1711-1731.
2. T. Inoue; A. Fujishima; S. Konishi; K. Honda. *Nature*, 1979, **277**, 637-638.
3. A. Crake; K. C. Christoforidis; A. Kafizas; S. Zafeiratos; C. Petit. *Applied Catalysis B: Environmental*, 2017, **210**, 131-140.
4. T. W. Woolerton; S. Sheard; E. Reisner; E. Pierce; S. W. Ragsdale; F. A. Armstrong. *Journal of the American Chemical Society*, 2010, **132**, 2132-2133.
5. T. W. Woolerton; S. Sheard; E. Pierce; S. W. Ragsdale; F. A. Armstrong. *Energy & Environmental Science*, 2011, **4**, 2393-2399.

6. J. Nunez; A. Víctor; P. Jana; J. M. Coronado; D. P. Serrano. *Catalysis Today*, 2013, **209**, 21-27. View Article Online
DOI: 10.1039/C9TA02793A
7. F. Yoshitomi; K. Sekizawa; K. Maeda; O. Ishitani. *ACS Applied Materials & Interfaces*, 2015, **7**, 13092-13097.
8. N. Zhang; S. Ouyang; T. Kako; J. Ye. *Chemical Communications*, 2012, **48**, 1269-1271.
9. A. Crake. *Materials Science and Technology*, 2017, **33**, 1737-1749.
10. R. Li; W. Zhang; K. Zhou. *Advanced Materials*, 2018, 1705512.
11. C. Wang; R. L. Thompson; P. Ohodnicki; J. Baltrus; C. Matranga. *Journal of Materials Chemistry*, 2011, **21**, 13452-13457.
12. F. Liao; Z. Zeng; C. Eley; Q. Lu; X. Hong; S. C. E. Tsang. *Angewandte Chemie International Edition*, 2012, **51**, 5832-5836.
13. S. Zhou; Y. Liu; J. Li; Y. Wang; G. Jiang; Z. Zhao; D. Wang; A. Duan; J. Liu; Y. Wei. *Applied Catalysis B: Environmental*, 2014, **158**, 20-29.
14. J. Lin; Z. Pan; X. Wang. *ACS Sustainable Chemistry & Engineering*, 2013, **2**, 353-358.
15. J. Qin; S. Wang; H. Ren; Y. Hou; X. Wang. *Applied Catalysis B: Environmental*, 2015, **179**, 1-8.
16. T. Ohno; N. Murakami; T. Koyanagi; Y. Yang. *Journal of CO2 Utilization*, 2014, **6**, 17-25.
17. X. Wang; K. Maeda; A. Thomas; K. Takanabe; G. Xin; J. M. Carlsson; K. Domen; M. Antonietti. *Nature Materials*, 2009, **8**, 76.
18. P. Niu; M. Qiao; Y. Li; L. Huang; T. Zhai. *Nano Energy*, 2018, **44**, 73-81.
19. Q. Liang; Z. Li; X. Yu; Z. H. Huang; F. Kang; Q. H. Yang. *Advanced Materials*, 2015, **27**, 4634-4639.
20. D. J. Martin; K. Qiu; S. A. Shevlin; A. D. Handoko; X. Chen; Z. Guo; J. Tang. *Angewandte Chemie International Edition*, 2014, **53**, 9240-9245.
21. M. Shen; L. Zhang; J. Shi. *Nanotechnology*, 2018, **29**, 412001.
22. W. Tu; Y. Xu; J. Wang; B. Zhang; T. Zhou; S. Yin; S. Wu; C. Li; Y. Huang; Y. Zhou. *ACS Sustainable Chemistry & Engineering*, 2017, **5**, 7260-7268.
23. Z. Sun; J. M. T. A. Fischer; Q. Li; J. Hu; Q. Tang; H. Wang; Z. Wu; M. Hankel; D. J. Searles; L. Wang. *Applied Catalysis B: Environmental*, 2017, **216**, 146-155.
24. J. Liu; S. Wen; Y. Hou; F. Zuo; G. J. Beran; P. Feng. *Angewandte Chemie*, 2013, **125**, 3323-3327.
25. M. Wang; M. Li; L. Xu; L. Wang; Z. Ju; G. Li; Y. Qian. *Catalysis Science & Technology*, 2011, **1**, 1159-1165.
26. X. Li; J. Zhao; J. Yang. *Scientific Reports*, 2013, **3**, 1858.

27. J. Pang; Y. Chao; H. Chang; H. Li; J. Xiong; M. He; Q. Zhang; H. Li; W. Zhu. *Journal of Colloid and Interface Science*, 2017, **508**, 121-128. View Article Online
DOI: 10.1039/C9TA02793A
28. Q. Weng; D. G. Kvashnin; X. Wang; O. Cretu; Y. Yang; M. Zhou; C. Zhang; D. M. Tang; P. B. Sorokin; Y. Bando. *Advanced Materials*, 2017, **29**.
29. S. Marchesini; A. Regoutz; D. Payne; C. Petit. *Microporous and Mesoporous Materials*, 2017, **243**, 154-163.
30. J. Kim; J. Han; M. Seo; S. Kang; D. Kim; J. Ihm. *Journal of Materials Chemistry A*, 2013, **1**, 1014-1017.
31. W. Lei; D. Portehault; R. Dimova; M. Antonietti. *Journal of the American Chemical Society*, 2011, **133**, 7121-7127.
32. L. Ci; L. Song; C. Jin; D. Jariwala; D. Wu; Y. Li; A. Srivastava; Z. Wang; K. Storr; L. Balicas. *Nature Materials*, 2010, **9**, 430.
33. J. Lu; K. Zhang; X. F. Liu; H. Zhang; T. C. Sum; A. H. C. Neto; K. P. Loh. *Nature Communications*, 2013, **4**, 2681.
34. L.-W. Yin; Y. Bando; D. Golberg; A. Gloter; M.-S. Li; X. Yuan; T. Sekiguchi. *Journal of the American Chemical Society*, 2005, **127**, 16354-16355.
35. C. Huang; C. Chen; M. Zhang; L. Lin; X. Ye; S. Lin; M. Antonietti; X. Wang. *Nature Communications*, 2015, **6**, 7698.
36. M. Zhou; S. Wang; P. Yang; C. Huang; X. Wang. *ACS Catalysis*, 2018, **8**, 4928-4936.
37. J. Li; N. Lei; H. Hao; J. Zhou. *Chemical Physics Letters*, 2017, **672**, 99-104.
38. K. Sivaprakash; M. Induja; P. G. Priya. *Materials Research Bulletin*, 2018, **100**, 313-321.
39. M. Florent; T. J. Bandosz. *Journal of Materials Chemistry A*, 2018, **6**, 3510-3521.
40. S. Alkoy; C. Toy; T. Gönül; A. Tekin. *Journal of the European Ceramic Society*, 1997, **17**, 1415-1422.
41. S. Marchesini; C. M. McGilvery; J. Bailey; C. Petit. *ACS Nano*, 2017, **11**, 10003-10011.
42. Y. Lin; J. W. Connell. *Nanoscale*, 2012, **4**, 6908-6939.
43. X.-F. Jiang; Q. Weng; X.-B. Wang; X. Li; J. Zhang; D. Golberg; Y. Bando. *Journal of Materials Science & Technology*, 2015, **31**, 589-598.
44. O. O. Kurakevych; V. L. Solozhenko. *Acta Crystallographica Section C: Crystal Structure Communications*, 2007, **63**, i80-i82.
45. Z. Yan; J. Lin; X. Yuan; T. Song; C. Yu; Z. Liu; X. He; J. Liang; C. Tang; Y. Huang. *Scientific Reports*, 2017, **7**, 3297.
46. M. Jedrzejczak-Silicka; M. Trukawka; M. Dudziak; K. Piotrowska; E. Mijowska. *Nanomaterials*, 2018, **8**, 605.

47. R. Geick; C. Perry; G. Rupprecht. *Physical Review*, 1966, **146**, 543.
48. R. Shankar; S. Marchesini; C. Petit. *The Journal of Physical Chemistry C*, 2018.
49. X. Gouin; P. Grange; L. Bois; P. L'Haridon; Y. Laurent. *Journal of Alloys and Compounds*, 1995, **224**, 22-28.
50. G. Ciofani; G. G. Genchi; I. Liakos; A. Athanassiou; D. Dinucci; F. Chiellini; V. Mattoli. *Journal of Colloid and Interface Science*, 2012, **374**, 308-314.
51. V. Cholet; L. Vandenbulcke; J. Rouan; P. Baillif; R. Erre. *Journal of Materials Science*, 1994, **29**, 1417-1435.
52. J. Riviere; Y. Pacaud; M. Cahoreau. *Thin Solid Films*, 1993, **227**, 44-53.
53. K. Park; D. Lee; K. Kim; D. Moon. *Applied Physics Letters*, 1997, **70**, 315-317.
54. A. S. Nazarov; V. N. Demin; E. D. Grayfer; A. I. Bulavchenko; A. T. Arymbaeva; H. J. Shin; J. Y. Choi; V. E. Fedorov. *Chemistry—An Asian Journal*, 2012, **7**, 554-560.
55. Y. Chen; J. Wang; Y. Chen; D. Liu; S. Huang; W. Lei. *Nanoscale*, 2018.
56. W. Lei; H. Zhang; Y. Wu; B. Zhang; D. Liu; S. Qin; Z. Liu; L. Liu; Y. Ma; Y. Chen. *Nano Energy*, 2014, **6**, 219-224.
57. L. A. Silva; S. C. Guerini; V. Lemos. *IEEE Transactions on Nanotechnology*, 2006, **5**, 517-522.
58. J. Wu; W. Zhang. *Solid State Communications*, 2009, **149**, 486-490.
59. R. Godin; Y. Wang; M. A. Zwijnenburg; J. Tang; J. R. Durrant. *Journal of the American Chemical Society*, 2017, **139**, 5216-5224.
60. F. M. Pesci; G. Wang; D. R. Klug; Y. Li; A. J. Cowan. *The Journal of Physical Chemistry C*, 2013, **117**, 25837-25844.
61. M. Marszewski; S. Cao; J. Yu; M. Jaroniec. *Materials Horizons*, 2015, **2**, 261-278.
62. Q. Sun; Z. Li; D. J. Searles; Y. Chen; G. Lu; A. Du. *Journal of the American Chemical Society*, 2013, **135**, 8246-8253.
63. S. Chen; P. Li; S. Xu; X. Pan; Q. Fu; X. Bao. *Journal of Materials Chemistry A*, 2018, **6**, 1832-1839.
64. D. C. Hurum; A. G. Agrios; K. A. Gray; T. Rajh; M. C. Thurnauer. *The Journal of Physical Chemistry B*, 2003, **107**, 4545-4549.
65. B. Choudhury; M. Dey; A. Choudhury. *Applied Nanoscience*, 2014, **4**, 499-506.
66. Y. Lei; L. Zhang; G. Meng; G. Li; X. Zhang; C. Liang; W. Chen; S. Wang. *Applied Physics Letters*, 2001, **78**, 1125-1127.
67. S. Koizumi; C. Nebel; M. Nesladek, *Physics and applications of CVD diamond*. John Wiley & Sons: 2008.
68. J. O. M. Bockris; B. E. Conway; R. E. White, *Modern aspects of electrochemistry*. Springer Science & Business Media: 2012; Vol. 22.

View Article Online
DOI: 10.1039/C9TA02793A

69. J. K. Stolarczyk; S. Bhattacharyya; L. Polavarapu; J. Feldmann. *ACS Catalysis*, [View Article Online](#)
2018, **8**, 3602-3635. [DOI: 10.1039/C9TA02793A](#)
70. S. Brunauer; P. H. Emmett; E. Teller. *Journal of the American Chemical Society*,
1938, **60**, 309-319.